# Large Eddy Simulation of Screech Tone Generation in a Planar Underexpanded Jet

Julien Berland, Christophe Bogey, Christophe Bailly

# Large Eddy Simulation of Screech Tone Generation in a Planar Underexpanded Jet

J. Berland*, C. Bogey† and C. Bailly‡

*Laboratoire de Mécanique des Fluides et d'Acoustique*
*École Centrale de Lyon & UMR CNRS 5509*
*69134 Ecully, France.*

**The screech tones generated by a three-dimensional planar underexpanded jet are computed directly using compressible large eddy simulation (LES). The jet operates at fully expanded Mach number $M_j = 1.55$, with Reynolds number $\mathrm{Re}_h = 6 \times 10^4$. The LES strategy is based on explicit selective filtering with spectral-like resolution, and low dispersion and low dissipation numerical algorithms are implemented to allow direct noise computation of the phenomenon. The investigation of the numerical results shows that the flow development, the shock cell structure and the upstream acoustic field are well reproduced by the computation. Flow visualization of shock/vortex interactions within the third shock-cell provides evidences that screech sound sources can be interpreted using the shock-leakage theory.**

## I. Introduction

Under certain operating conditions, supersonic over- and under-expanded jets can produce discrete frequency sounds, referred to as screech tones, dominating all other noise sources in the forward direction. This phenomenon was first observed in the 1950s by Powell,[1] who proposes that the screech production is controlled by a feedback loop. Indeed, the interactions of the turbulent motions developing in the jet shear-layers with the shock waves of the quasi-periodic shock-cell system may give rise to upstream-propagating acoustic waves. These waves are reflected back at the nozzle lip, and excite the shear-layer, closing the resonant loop.

Since the first observations of Powell, a large number of experimental and theoretical studies have been carried out, and knowledge has been gained on the self-sustained loop characteristics. One may refer for instance to the review of Raman[2] for further details. Current understanding of the screech is nevertheless primarily qualitative, and quantitative predictions are limited to the fundamental frequency at which the phenomenon occurs. In particular, there is no theory that permits to determine the amplitude of the upstream-propagating acoustic fluctuations. Such a prediction relies on a clear understanding of the sound production due to shock/vortex interactions inside the shear-layer. Recent works by Suzuki & Lele[3] introduced geometrical acoustics to model the sound generation process. An analogy between ray trajectory inside the jet and shock deformation may indeed be drawn. The theory of Suzuki & Lele[3] showed that shocks tend to leak through the shear-layer near the saddle points of vortices. This process moreover results in production of sound waves with shapes similar to that of the screech tones. However, the study of Suzuki & Lele[3] has been accomplished for a single shock interacting with a shear-layer. Experimental evidences of the shock-leakage phenomenon are not available so far, but numerical simulations can now help toward demonstrating that shock-leakage occurs in screeching jet.

Simulation of jet screech noise has indeed become recently feasible. Nevertheless, such computation remains a challenging issue: the self-sustained aeroacoustic loop responsible for screech tones leads to a strong coupling between the aerodynamic and the acoustic fluctuations, and both fields must therefore be

*PhD Student, julien.berland@ec-lyon.fr
†Research scientist CNRS, christophe.bogey@ec-lyon.fr
‡Professor of Ecole Centrale de Lyon, christophe.bailly@ec-lyon.fr

resolved within a same run. This method, referred to as Direct Noise Computation (DNC), has in addition difficulty dealing with shock-associated noise simulations because it requires discretization algorithms with high-order properties. Such simulations must compute shock waves while being able to resolve the full range of length and amplitude scales associated with aerodynamic and acoustic fluctuations, and non-reflecting boundary conditions for both turbulent motions and sound waves have to be implemented.

Shen & Tam[4] solved for example the unsteady Reynolds Averaged Navier-Stokes (URANS) equations to reproduce the screech tones of circular jets. Their method however provides a phase-averaged solution at the forcing frequency induced by the screech, and thus simulates a limited bandwidth of the turbulence spectra. The full range of turbulence scales can be obtained by Direct Numerical Simulations (DNS). The required computational effort is unfortunately very important, and flow investigation using DNS is generally restricted to low Reynolds number phenomena. In an attempt to study shock-associated noise, Suzuki & Lele[3] have for instance performed the DNS of a supersonic shear-layer impinging on an oblique compression wave, with the aim of providing an insightful investigation of the shock-leakage phenomena. However, such a DNS can hardly be extended to a complete shock-containing supersonic jet. The study of flows with Reynolds number of practical interest, and of their radiated acoustic fields may be performed using compressible large eddy simulation (LES). Indeed, in LES, only the larger scales are resolved and a subgrid scale model takes into account the influence of smaller unresolved wavelengths. It is therefore possible to deal with realistic turbulence configurations while keeping computational cost at a reasonable level. Feasibility of DNC of subsonic jets using LES has been demonstrated for instance by Bogey & Bailly[5–7] or Bodony & Lele.[8] As for supersonic jet noise, Al Qadi & Scott[9] performed the LES of a rectangular jet exhibiting screech tones, the shocks being captured with a high-order filter combined to a TVD (Total Variation Diminishing) time integration scheme. Imamoglu & Balakumar[10] carried out the computation of a shock-containing circular jet using implicit LES based on WENO (weighted essentially non oscillatory) spatial discretization techniques, and on a TVD algorithm for time advancement. Loh *et al.*[11] also simulated the screech tones of a circular jet using a low-order finite volume method. The simulations above however involve shock capturing or low-order algorithms, and these methods have been shown not to be well suited for LES because they may introduce excessive dissipation on the resolved scales,[12] or generate numerical errors with large magnitude.[13] The alternative is thus to perform a LES relying only on low dispersion and low dissipation algorithms, which ensure numerical accuracy while avoiding significant artificial damping of the wavelengths accurately resolved.

The objectives of the present work are twofold. First, in order to show the feasibility of the DNC of screech tones using high-order algorithms, the compressible LES of a planar shock-containing jet is performed. The jet operates at underexpanded conditions so that a quasi-periodic shock cell structure is formed in the jet plume. The Reynolds number based on the fully expanded jet Mach number $M_j = 1.55$, and on the jet height $h = 3$ mm, is equal to $6 \times 10^4$. The LES approach is based on low dispersion and low dissipation numerical methods,[14,15] and selective filtering is applied explicitly to take into account the effects of subgrid scales.[16] The computation aims at reproducing the aerodynamic flow development and the features of the screech tones. Once consistency of the simulation is demonstrated, the results are used to provide numerical evidences of the shock-leakage phenomenon due to shock/vortex interactions.

The outline of the paper is the following. The numerical procedure and the simulation parameters are detailed in section II. The turbulent flow development and the acoustic field of the LES are then investigated in section III. Flow visualizations of shock/vortex interactions in the shear-layer are finally depicted in section IV to provide evidences of the connection between the shock-leakage process and the sound sources of the screech tones. Concluding remarks are drawn in section V.

## II. Numerical procedure

### A. LES strategy and numerical methods

The filtered compressible Navier-Stokes equations written in the form proposed by Vreman *et al.*[17] are solved to perform the LES of a three-dimensional planar underexpanded jet. To take account of the dissipation provided by the unresolved scales, an eddy-viscosity-based model is commonly introduced. This modeling approach may nevertheless introduce excessive dissipation on the resolved scales, leading to a decrease of the effective Reynolds number of the simulation.[18] An alternative to eddy-viscosity models consists in minimizing the dissipation on the resolved scales. Explicit selective high-order filtering of the flow variables is therefore applied to diffuse energy only at the smaller resolved scales, close the grid cut-off wave number.

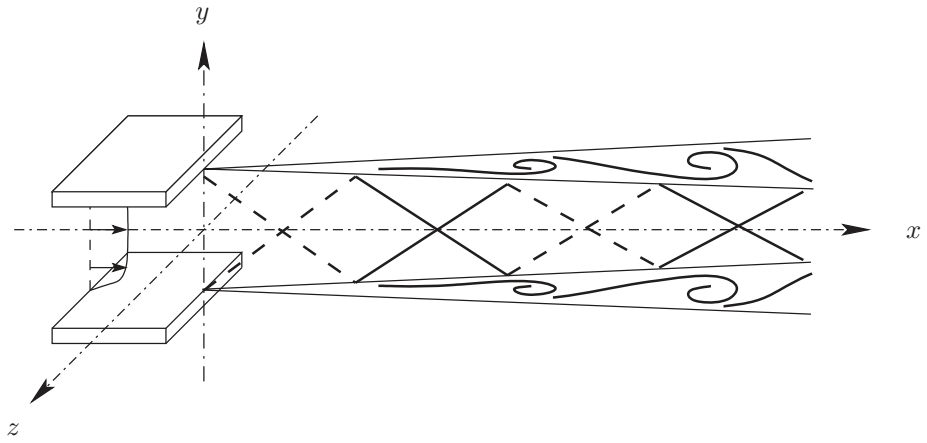


**Figure 1. Sketch of the computational domain and of the coordinate system.**

The method has been successfully used in recent applications[5–7,19] and is used here to compute the turbulent flow development and the acoustic field of a planar supersonic shock-containing jet.

Low dispersion and low dissipation explicit numerical schemes designed on 11 points[14] are used for spatial discretization, and time integration is carried out by a fourth order low-storage Runge-Kutta scheme.[15] Periodic boundary conditions are implemented in the $z$-direction while non-reflecting conditions of Tam & Dong[20] are used in the $x$ and $y$ directions so that acoustic perturbations leave the computational domain without the generation of significant spurious waves. In addition, a sponge zone is set up at the outflow in order to attenuate aerodynamic fluctuations before they reach the downstream limit of the domain. The jet nozzle, which is known to be necessary for screech tone emergence, is described by two parallel adiabatic plates separated by a distance $h$ defining the jet height. Inside the nozzle, characteristics[21] are implemented to specify the inflow conditions. A sketch of the computational domain and of the coordinate system is given in figure 1.

## B. Simulation parameters

### *1. Inflow conditions*

The jet is assumed to be supplied by a convergent nozzle whose designed Mach number $M_d$ is therefore equal to 1. The ambient region surrounding the flow is at rest and characterized by a pressure $p_\infty = 10^5$ Pa and a density $\rho_\infty = 1.22$ kg.m$^{-3}$. Reservoir temperature $T_r$ is set to 288 K, and an elevated pressure $p_e/p_\infty = 2.09$ is imposed inside the nozzle so that the jet operates at underexpanded conditions. The fully expanded jet Mach number $M_j$, defined by,

$$M_j = \left\{ \frac{2}{\gamma - 1} \left[ \left( 1 + \frac{\gamma - 1}{2} M_d^2 \right) \left( \frac{p_e}{p_\infty} \right)^{1-1/\gamma} - 1 \right] \right\}^{1/2} \tag{1}$$

is then equal to 1.55. This value has indeed been observed by Krothapalli *et al.*[22] to correspond to maximum screech sound radiation for a rectangular jet with a large aspect ratio.

Inside the nozzle, flow variables are uniform except near the walls where the no-slip condition is required. Boundary layer profiles are therefore implemented close to the solid surfaces using an approximation of the laminar Blasius solution, given by,

$$\frac{u}{U_e} = \begin{cases} \eta(2 - 2\eta^2 + \eta^3) & \text{if} \quad \eta < 1 \\ 1 & \text{if} \quad \eta \geq 1 \end{cases} \tag{2}$$

where $\eta$ is the distance to the wall normalized by the boundary layer thickness $\delta$, and $U_e = 310$ m.s$^{-1}$ is the designed nozzle velocity. The inflow density profile is then given by the Crocco-Busemann relation:

$$\rho = \left[ \frac{1}{\rho_w} - \left( \frac{1}{\rho_w} - \frac{1}{\rho_e} \right) \frac{u}{U_e} - \frac{\gamma - 1}{2} M_d^2 \left( \frac{u}{U_e} - 1 \right) \frac{u}{U_e} \right]^{-1} \tag{3}$$

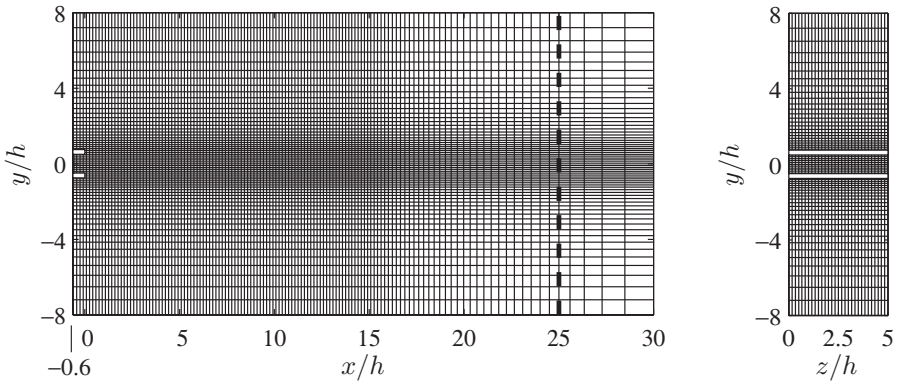


**Figure 2. View of the Cartesian mesh in the planes ($xy$) and ($yz$). Only one point over four are plotted. The dashed line stands for the beginning of the sponge zone and the white surfaces are the nozzle lips.**

where the density on the walls $\rho_w$ can be evaluated by the perfect gas relationship $\rho_w = p_e/rT_r$. For high Reynolds number ($\sim 10^5$), boundary layers are generally very thin[23] with a momentum thickness $\delta_\theta/h$ of the order of $10^{-3}$. However, to perform a computation with an affordable number of grid points, $\delta_\theta/h$ is set in this work to a larger value: $3 \times 10^{-2}$.

The jet height is $h = 3$ mm and the nozzle lip thickness $h_l$ is similar to the one used in the experiments of Raman & Rice,[24] that is $h_l = h/4$. The Reynolds number $\mathrm{Re}_h = U_j h/\nu$ is then $6 \times 10^4$, where $U_j = M_j c_j$ with $c_j = 278$ m.s$^{-1}$.

*2. Numerical parameters*

The computational domain is discretized by a Cartesian grid of $525 \times 257 \times 121 \sim 16.3 \times 10^6$ points. The smallest mesh size $\Delta_m = h/40$ allows to use 40 mesh points within the jet height and 7 nodes inside the boundary layer. The grid is presented in Figure 2 and the domain of interest, which excludes the sponge zone, has the following dimensions: $25.6h \times 16h \times 5h$, with a nozzle extending over $0.6h$ inside the domain. The time step $\Delta t \simeq 8.6 \times 10^{-8}$ corresponds to a CFL $= (U_j + c_j)\Delta t/\Delta_m$ number equal to 1, and selective filtering is applied every iteration. To ensure statistical convergence and to compute at least one hundred periods of the screech loop, the simulation is run over 80,000 time steps. Simulation parameters are given in table 2.

## III. Results and validation

### A. Instantaneous vorticity and pressure

An instantaneous snapshot of isosurfaces of the spanwise vorticity $\omega_z$ in the whole computational domain is represented in figure 3. A large range of turbulence scales, especially the fine scales characterizing high Reynolds number flows, are observed. Pressure isocontours in the plane $z/h = -2.5$ are also reported. Upstream-propagating wavefronts are clearly visible on either side of the jet. This acoustic radiation is typical of screech tones, and it will be shown in section D that the phenomenon is locked on a frequency denoted $f_s$, whose Strouhal number $\mathrm{St} = f_s h/U_j$ is equal to 0.126.

**Table 1. Parameters used for the LES of the three-dimensional planar underexpanded jet.**

| $M_j$ | $p_e/p_\infty$ | $h$ (mm) | $h_l$ | $\delta_\theta/h$ | $\mathrm{Re}_h$ | $\Delta_m$ | $\Delta t$ (s) |
|---|---|---|---|---|---|---|---|
| 1.55 | 2.09 | 3 | $h/4$ | $3 \times 10^{-2}$ | $6 \times 10^4$ | $h/40$ | $8.6 \times 10^{-8}$ |

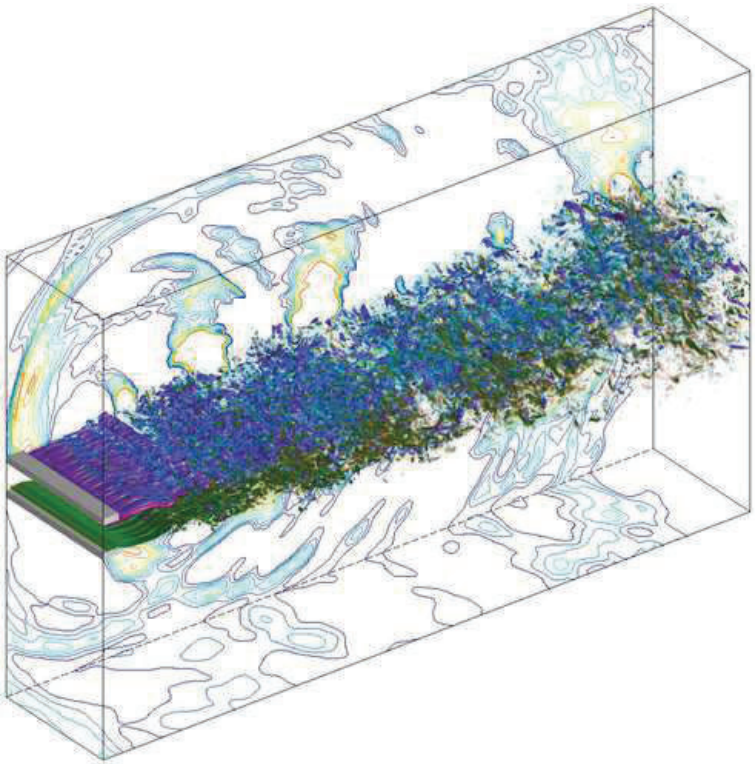

**Figure 3. Instantaneous snapshot of spanwise vorticity $\omega_z$ in the whole computational domain and of pressure in the plane $z/h = -2.5$. The nozzle lips are represented in gray.**

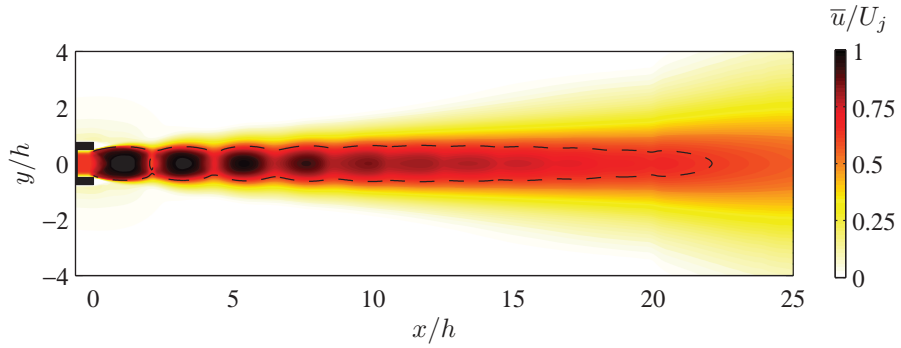


**Figure 4. Colormap of the normalized mean streamwise velocity $\overline{u}/U_j$ in the central $(x, y)$-plane. − − − , sonic line ($M = 1$). The black rectangle represents the nozzle lips.**

## B. Mean flow field

### *1. Global mean flow*

A colormap of the normalized mean streamwise velocity $\overline{u}/U_j$ in the central $(x, y)$-plane is shown in figure 4. Due to the overpressure at the nozzle exit, five shock-cells exhibiting the distinctive bow-shape structure are apparent in the jet plume for $x/h < 10$. In addition, a decrease of the axial velocity and a weakening of the shock strength in the downstream direction is observed. The interactions between the cells and the shear-layer are indeed stronger as the vortical structures develop in the streamwise direction. The velocity and pressure gradients induced by the shocks are consequently smoothed out. Also shown in figure 4 is the supersonic core of the jet, whose boundary is defined by the sonic line (points where the Mach number $M$ is 1). This region extends down to $x/h = 22$ which is somewhat larger than the value of $x/h = 15$ measured by Krothapalli *et al.*[22] for a large-aspect-ratio rectangular jet operating at $M_j = 1.52$. This discrepancy may

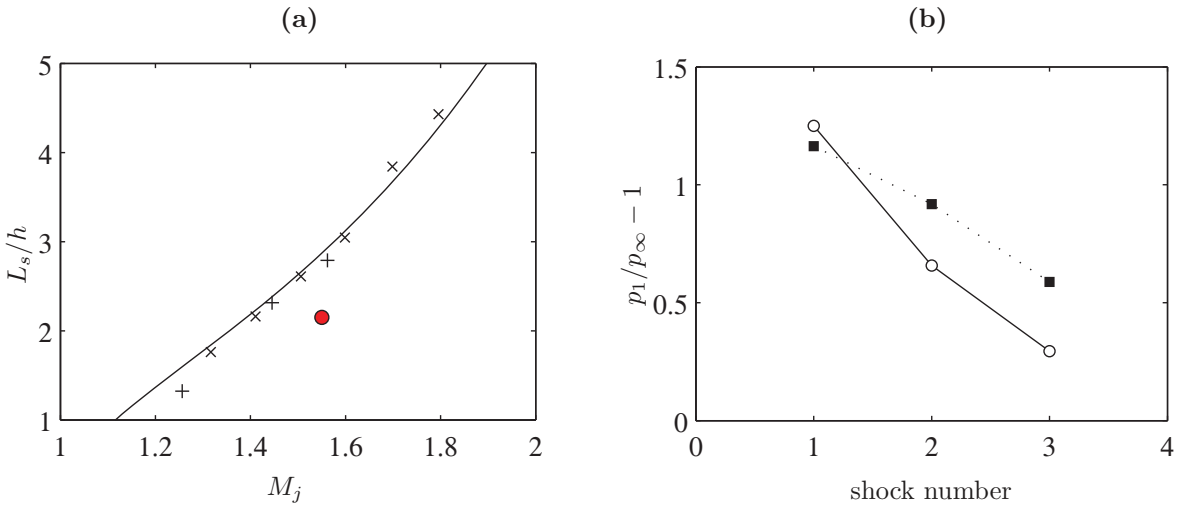


**Figure 5. (a) Shock-cell spacing $L_s/h$ as a function of the fully expanded jet Mach number $M_j$. Measurements on rectangular jets: +, Raman & Rice;[24] ×, Panda *et al.*[25] ———, analytical solution of Tam[26] for a plane jet. ●, present computation. (b) Shock strength $p_1/p_\infty - 1$ for the first three shock-cells ($p_1$ is the pressure upstream the shock). ——○——, Raman[28] measurements on a $M_j = 1.55$ rectangular jet; ·····■·····, present computation.**

be attributed to the turbulent development of the jet. The initial shear layer of the jet simulated by LES is laminar and relatively large. The shear-layer at the nozzle exit of the experiments of Krothapalli *et al.*[22] is however probably thinner and turbulent, which may lead to a faster jet development and to a stronger decay of the mean centerline velocity with respect to the simulation.

### *2. Shock-cell structure*

Average shock-cell spacing deduced from the LES mean flow data is presented in figure 5.a, where the shock-cell spacing $L_s/h$ is plotted as a function of the fully expanded jet Mach number $M_j$ for various experiments on rectangular jets. The shock-cell spacing provided by the computation appears to be slightly smaller than expected. This trend may be explained by the initial shear-layer thickness used for the calculation. Indeed, according to Tam,[26] the jet column acts as a waveguide for flow discontinuities, and the successive reflections of shocks and expansion waves on the sonic line give rise to the periodic shock-cell structure. Shock spacing is therefore related to the height of the supersonic core, which is relatively small for the present LES due to the thickness of the shear-layer. The supersonic core height at the nozzle exit is more precisely $h^* \simeq 0.8h$. The normalized shock cell-spacing $L_s/h^*$ is then equal to 2.7, which is in better agreement with the experimental results shown in figure 5.a. This trend is in addition supported by the shock cell model of Morris & Baht,[27] which shows in particular that shock spacing of round jets decreases when the mixing layer thickness is increased.

The strength $(p_1/p_\infty - 1)$, where $p_1$ is the mean pressure just upstream of the shock, of the first three shocks of the simulation are compared in figure 5.b to the measurements of Raman[28] observed for a supersonic rectangular jet at the same Mach number. The strength of the first shock is found to agree with the result of Raman,[28] whereas the second and the third shocks exhibit a larger pressure gap. The overestimation of the shock strengths have two origins. First, as it has been reported above in this section, the nozzle inflow conditions implemented for the LES probably induce a slower turbulent flow development, implying a slower weakening of the shocks compared to the experiment of Raman.[28] One may also argue that shear-layer development in the major-axis plane of rectangular jets contributes to three dimensional shock-cell structures,[29] whereas for planar jet the mean flow is homogeneous in the spanwise direction. This observation could support the fact that the first shock is similar in rectangular and planar jets. However, further downstream, the three-dimensional structure of the jets should differ, resulting in discrepancies between shock strengths.

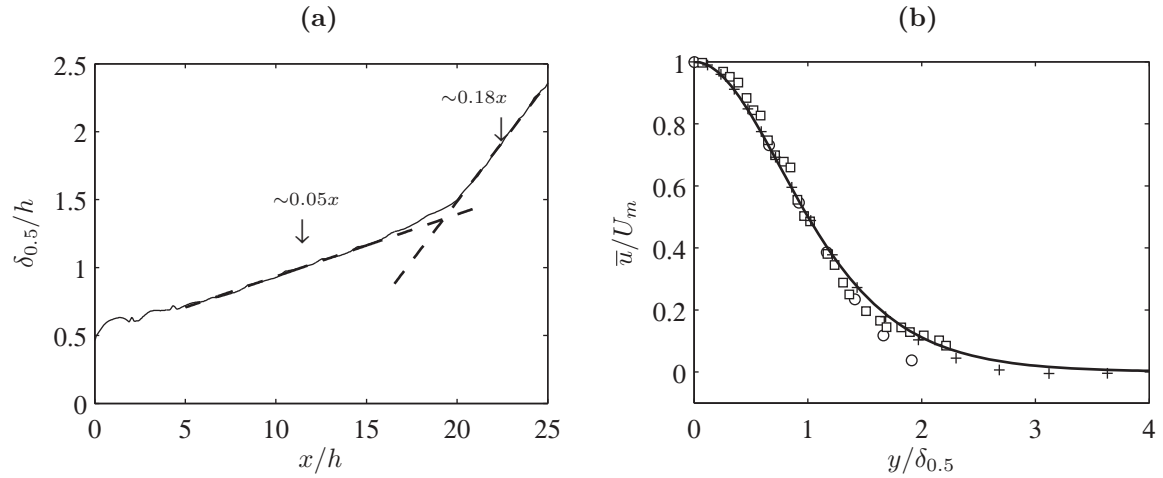


**Figure 6. (a) Jet half-width $\delta_{0.5}/h$ as a function of the downstream position $x/h$. (b) Transverse profile of the mean axial velocity $\overline{u}/U_m$ normalized by the centerline velocity as a function of $y/\delta_{0.5}$. ———, profile given by (4); ○, Gutmark & Wygnanski;[30] □, Bradbury;[31] +, present computation at $x/h = 25$.**

*3. Mean velocity distribution*

Figure 6.a presents the axial evolution of the jet half-width $\delta_{0.5}/h$. In the upstream part of the jet, for $x/h < 5$, the jet half-width is modulated by the expansion and compression waves of the first two shock-cells. Between $x/h = 5$ and $x/h = 15$, the jet spreads apparently linearly so that we can write $\delta_{0.5} = k(x - x_0)$, where $k$ is the spreading rate and $x_0$ the virtual origin. Thus, for $5 < x/h < 15$, the rate is relatively small and equal to 0.05. Further downstream at $x/h = 20$, large vortical structures begin to appear, and the spreading rate increases and reaches the value of 0.18. This value is consistent with the measurements of Krothapalli *et al.*[22] which provide a spreading rate of 0.16 for a $M_j = 1.52$ rectangular jet, in the downstream region for $40 < x/h < 80$.

The transverse profile of the mean axial velocity $\overline{u}/U_m$ normalized by the centerline velocity is given in figure 6.b as a function of $y/\delta_{0.5}$. Also shown in figure 6.b are the experimental results of Gutmark & Wygnanski[30] and Bradbury,[31] and the analytical self-similar profile for a plane jet :

$$\frac{\overline{u}}{U_m} = \frac{1}{\cosh^2(0.88 y/\delta_{0.5})} \tag{4}$$

The various profiles appear to collapse very well over the whole transverse range.

## C. Shear-layer oscillation modes

The shear-layer development is now investigated using velocity fluctuations provided by the LES, with the aim of characterizing the development of the aerodynamic instabilities.

*1. Dominant instability modes*

The axial evolution of the instability modes is first studied. Spectra of axial and transverse velocity perturbations $u'$ and $v'$ are computed in the shear-layer along the line $(x, y = h/2, z = 0)$, as shown in figure 7 where the location of the measurement points are reported. The streamwise development of the power spectral density of the velocity component $u'$ is depicted in figure 8.a as a function of the axial position $x/h$ in term of a colormap (in logarithmic scale). In the upstream part of the flow, for $x/h < 10$, the dominant mode is observed to be locked on the screech Strouhal number $\mathrm{St} = 0.126$. In addition, the amplitude of velocity fluctuations for this mode exhibits a significant modulation by the shock-cells structure, which is indicated by the successive decrease and recovery of the power spectral level close the shocks. Further downstream, for $x/h > 15$, the instability at the screech frequency vanishes, and a lower-frequency mode with a broader spectral distribution is seen to develop in the shear layer. The peak frequency is moreover shown to slightly decrease with $x/h$. The corresponding Strouhal number is indeed equal to 0.054 in $x/h = 15$, and to 0.036 in $x/h = 25$. Note that these frequencies are not sub-harmonic of the screech tones.

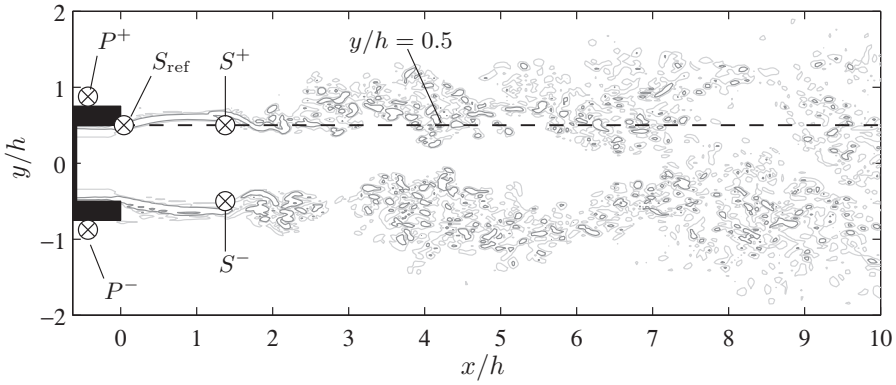


**Figure 7. Definition of the measurement points in the central $(x, y)$-plane.**

The axial evolution of the power spectral density of $v'$ is now presented in figure 8.b. Similarly to the velocity component $u'$, the dominant oscillation mode of the shear-layer occurs at the fundamental screech frequency. The mode nevertheless shows a weaker modulation by the shocks and it is in addition clearly observed up to $x/h = 22$. For $x/h > 15$, a low frequency mode similar to the one observed for $u'$ emerges, but with a fairly constant Strouhal number, equal to 0.045 at $x/h = 25$.

*2. Transverse symmetry of the modes*

Screech instability modes identified in the upstream part of the jet may be classified using the interpretation reported by Thomas & Prakash[32] of the sinuous and varicose instabilities of the planar jet. Cross-spectra of the velocity fluctuations on either the jet, in the shear-layer, are therefore determined using the data at the locations $(x/h, y/h) = (1.3, 0.5)$ and $(x/h, y/h) = (1.3, -0.5)$, as shown in figure 7 by the points $S^+$ and $S^-$. The cross-spectrum based on the axial perturbations $u'$ is denoted $P_{uu}$, while $P_{vv}$ is the cross-spectra determined from $v'$. The quantities deduced from the cross-spectrum are the amplitudes $|P|$, the coherence functions $C$ and the phases $\varphi$ which are respectively provided in figures 9.a1, 9.a2 and 9.a3 for the axial velocity fluctuations $u'$, and in figures 9.b1, 9.b2 and 9.b3 for the transverse perturbations $v'$.

The amplitude $|P_{uu}|$ shows four harmonic peaks whose fundamental corresponds to the screech frequency. In addition, the coherence function $C_{uu}$ appears to be close to 1 for these four frequencies, demonstrating that they are coherent on either side of the jet. The phase $\varphi_{uu}$, which indicates the phase difference between fluctuations in $y = h/2$ and $y = -h/2$, shows that the fundamental ($f_s$) and the second ($3f_s$) harmonics are antisymmetric, whereas the first ($2f_s$) and the third ($4f_s$) harmonics are symmetric. It is indeed observed that $\varphi_{uu}(f_s) = -\pi$, $\varphi_{uu}(2f_s) = 0$, $\varphi_{uu}(3f_s) = \pi$ and $\varphi_{uu}(4f_s) = 0$.

Consider now the cross-spectrum calculated from the transverse fluctuations $v'$, it is found that the amplitude $|P_{vv}|$ is similar to that obtained for $u'$. A series of harmonic peaks are visible in figure 9.b1, and are coherent since the coherence function $C_{vv}$ displays a large value ($> 0.8$) for these frequencies. The cross-spectrum phase $\varphi_{vv}$ is nevertheless different from $\varphi_{uu}$. The fundamental ($f_s$) and the second ($3f_s$) harmonics are symmetric, while the first ($2f_s$) and the third ($4f_s$) are antisymmetric. Phase difference in figure 9.b3 is indeed such as $\varphi_{vv}(f_s) = 0$, $\varphi_{vv}(2f_s) = -\pi$, $\varphi_{uu}(3f_s) = 0$ and $\varphi_{uu}(4f_s) = \pi$.

It can be finally deduced from the phase differences on either side of the jet that the oscillation modes at the screech fundamental frequency ($f_s$) and at the second harmonic ($3f_s$) are sinuous instabilities, whereas the jet undergoes a varicose mode at the first ($2f_s$) and third ($4f_s$) harmonic frequencies. It should be noted that the oscillation modes at $f_s$, $2f_s$ and $3f_s$ identified by Raman & Rice[24] on a screeching rectangular jet have the same phase distribution.

A similar investigation has been carried out for the low frequency mode observed in the downstream region of the jet, for the transverse velocity fluctuations $v'$. The cross-spectrum $P_{vv}$ is therefore now computed between the points at $(x/h, y/h) = (22.5, 0.5)$ and $(x/h, y/h) = (22.5, -0.5)$. The amplitude $|P_{vv}|$, the coherence function $C_{vv}$ and the phase $\varphi_{vv}$ are respectively plotted in figures 10.a, 10.b and 10.c. A peak at Strouhal number $\text{St} = fh/U_j = 0.045$ can be seen in the plot of the amplitude $|P_{vv}|$. The coherence

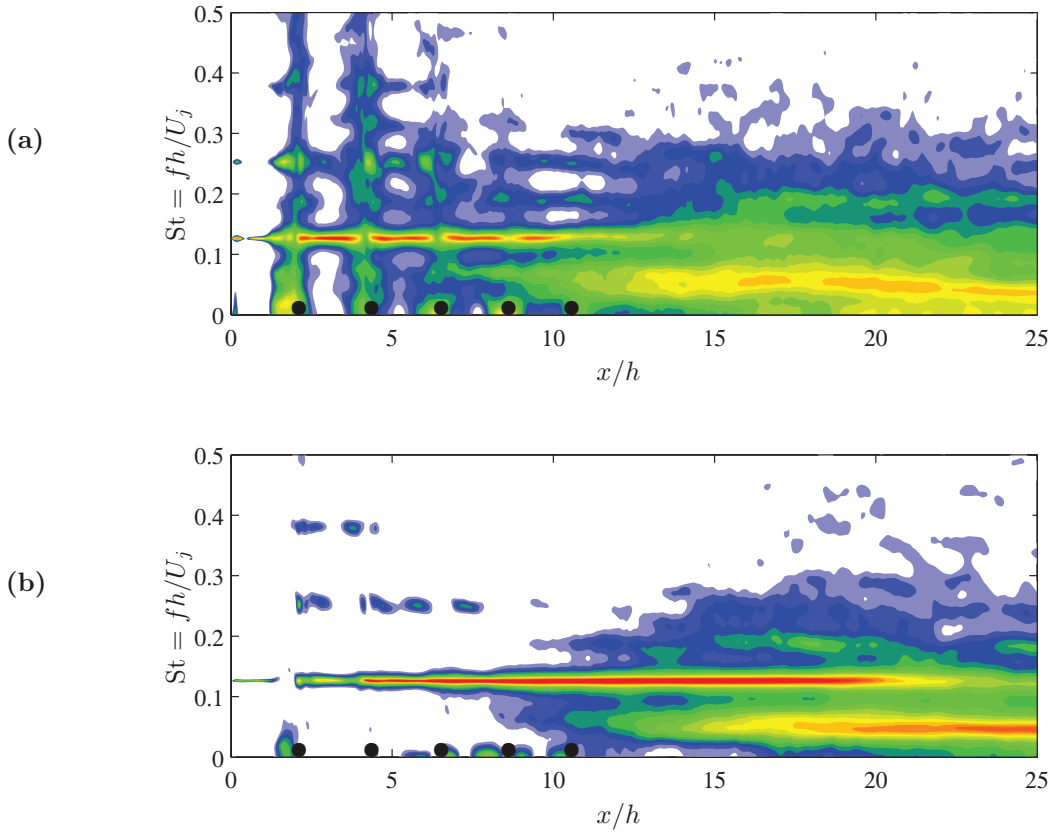


**Figure 8. Streamwise development of the power spectral density of the velocity fluctuations in the shear-layer, along the line $(x, y = h/2, z = 0)$, in logarithmic scales. (a) Axial perturbations $u'$ and (b) transverse fluctuations $v'$. The shock locations deduced from the mean-flow are represented by the symbols •.**

function at this frequency is about 0.85, and is large enough to conclude that the velocity perturbations are correlated on either side of the jet. The phase difference $\varphi_{vv}$ then demonstrates that the low frequency oscillation mode is symmetric, as $\varphi_{vv} = 0$ at St $= 0.045$. The shear-layer consequently exhibits a flapping instability mode in the downstream part of the jet.

### *3. Convection velocity*

The convection velocities of the screech oscillation modes inside the shear-layer are now determined. The axial phase variation $\Delta\varphi$ of the coherent mode is computed using the cross-spectra of the velocity component $u'$ between measurement points on the line $(x, y = h/2, z = 0)$ and a reference point located at $(x/h, y/h) = (0.05, 0.5)$. The phase evolution is presented in figure 11 as a function of $x/h$ for the fundamental and the first harmonic of the screech. The relative phase, which is observed to increase regularly in the downstream direction, indicates a convection process. The average convection velocity $u_c$ is then given by $u_c = 2\pi f/\alpha$, where $f$ is the mode frequency and $\alpha$ the slope of the least-square straight line fit of the curve $\Delta\phi$. Convection velocities are found to be $u_c = 0.57U_j$ for the fundamental, and $u_c = 0.51U_j$ for the first harmonic. These values are in agreement with the experimental data of Raman & Rice[24] which provide $u_c = 0.54U_j$ and $u_c = 0.56U_j$ for the instabilities at the screech frequency and at the first harmonic, for a $M_j = 1.44$ rectangular jet.

### *4. Spanwise structure*

The spanwise structure inside the shear-layer is identified by computing space-time velocity correlations inside the shear-layer. The spanwise correlation coefficient based on the axial velocity fluctuations $u'$ is

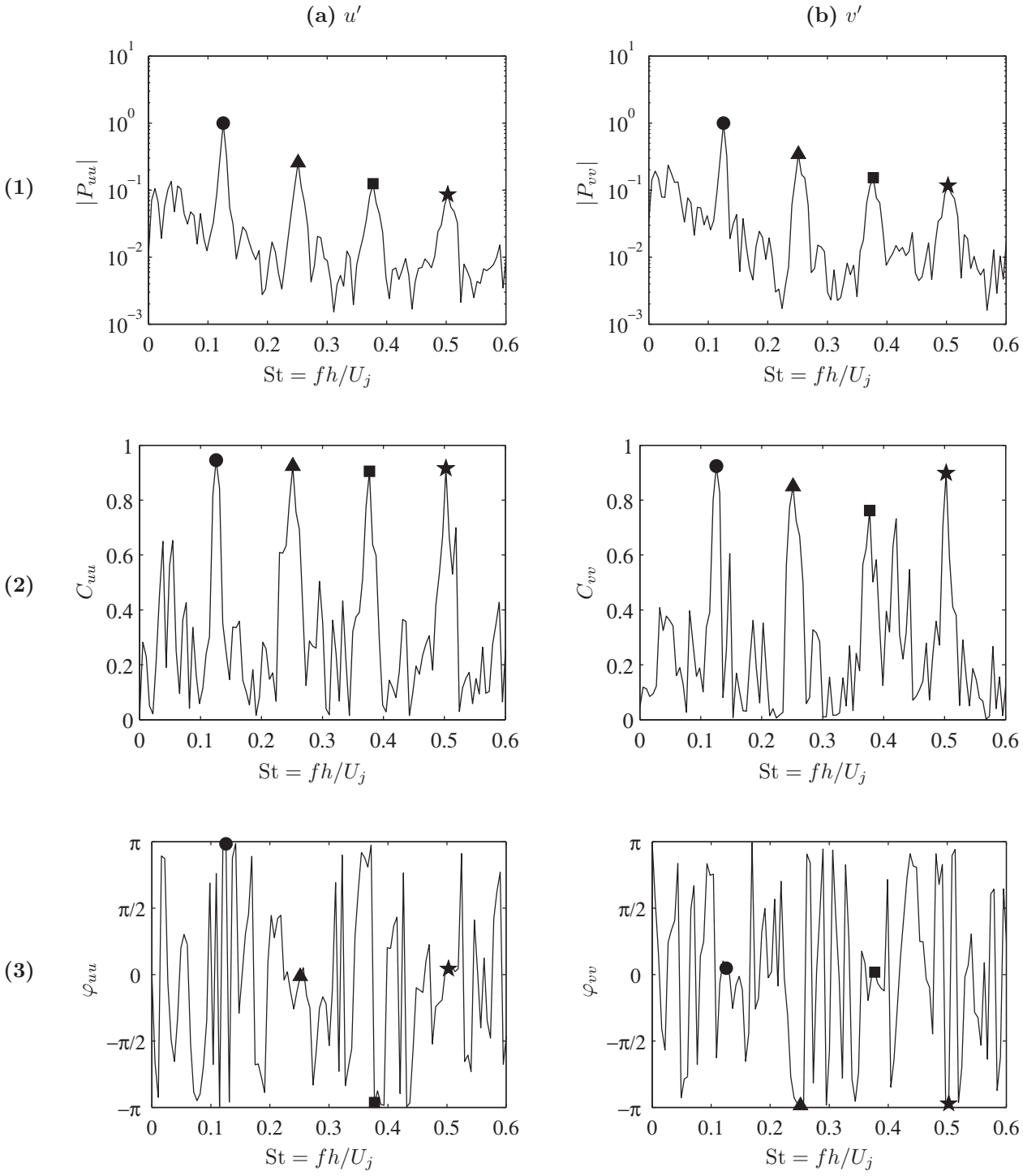


**Figure 9. Cross-spectra of the velocity fluctuations on either side of the jet, in $(x/h, y/h) = (1.3, 0.5)$, and $(x/h, y/h) = (1.3, -0.5)$, as functions of the Strouhal number $\mathrm{St} = fh/U_j$. •, screech frequency ($f_s$); ▲, 1st harmonic ($2f_s$); ■, 2nd harmonic ($3f_s$); ⋆, 3rd harmonic ($4f_s$). (a), Cross-spectrum of the axial velocity perturbations $u'$; (b), cross-spectrum of the transverse velocity perturbations $v'$. (1), Amplitude $|P|$; (2), coherence function $C$; (3), phase $\varphi$.**

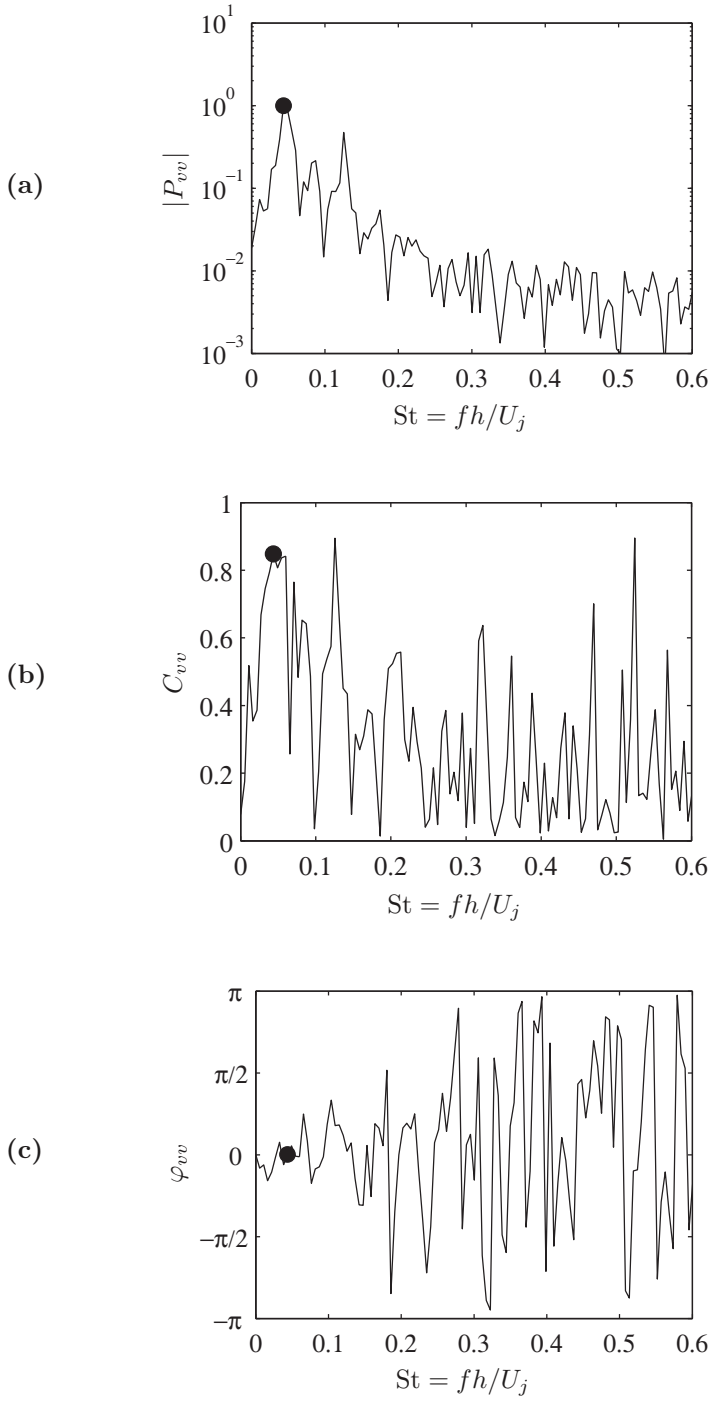


**Figure 10. Cross-spectrum of the velocity fluctuations on either side of the jet, in $(x/h, y/h) = (22.5, 0.5)$, and $(x/h, y/h) = (22.5, -0.5)$, as a function of the Strouhal number $\mathrm{St} = fh/U_j$. •, $\mathrm{St} = 0.045$. (a), Amplitude $|P_{vv}|$; (b), coherence function $C_{vv}$; (c), phase $\varphi_{vv}$.**

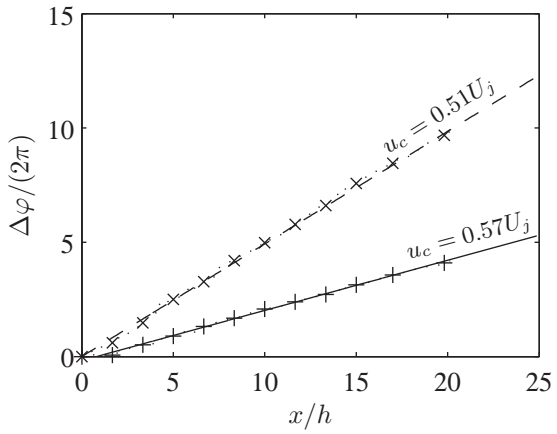


**Figure 11. Phase variation $\Delta\varphi/(2\pi)$ with axial distance $x/h$ of the velocity fluctuations $u'$ for the fundamental and the first harmonic screech modes, on the line $y = h/2$ ($z/h = 0$). $\cdots+\cdots$, fundamental ($f_s$); $\cdots\times\cdots$, first harmonic ($2f_s$).**

defined at $\mathbf{x}$, as,

$$R_{uu}(\mathbf{x}, r_z, \tau) = \frac{\overline{u'(\mathbf{x},t)u'(\mathbf{x}+r_z\mathbf{e}_z,t+\tau)}}{\left[\overline{u'^2(\mathbf{x},t)}\ \overline{u'^2(\mathbf{x}+r_z\mathbf{e}_z,t)}\right]^{1/2}} \tag{5}$$

where $\mathbf{e}_z$ is the unit vector associated with the $z$-direction, $r_z$ the spanwise separation, $\tau$ the time lag and $\overline{\cdot}$ the statistical average. The coefficient $R_{vv}(\mathbf{x}, r_z, \tau)$ is computed in a similar manner for the transverse perturbations $v'$.

The coefficients $R_{uu}$ and $R_{vv}$ are determined at two locations in the shear-layer. The first measurement position is located in the upstream part of the jet, at $(x/h, y/h, z/h) = (5, 0.5, 0)$, in order to investigate the screech oscillation mode. The second point is situated further downstream, at $(x/h, y/h, z/h) = (22.5, 0.5, 0)$, in order to identify the low frequency mode observed in the spectra of figures 8.a and 8.b. Results obtained at $(x/h, y/h, z/h) = (5, 0.5, 0)$ are plotted in figures 12.a and 12.b for $R_{uu}$ and $R_{vv}$, respectively, while figures 12.c and 12.d present the coefficients $R_{uu}$ and $R_{vv}$ at $x/h = 22.5$. Note that in these figures, the time lag $\tau$ is normalized by the screech period $T_s$, and that $r_z$ is restricted to the interval $[-2.5h, 2.5h]$, which corresponds to the domain extent in the spanwise direction.

Consider first the results at $x/h = 5$. As expected, the maximum correlation occurs at $(r_z, \tau) = (0, 0)$, where $R_{uu} = R_{vv} = 1$. Both correlation coefficients $R_{uu}$ and $R_{vv}$ then quickly decrease as the spanwise separation or the time lag are increased, suggesting the existence of small-scale spatially coherent structures. However, the correlation coefficients do not fall down to zero for large space-time shifts. For instance, for $\tau = 0$, $R_{uu}$ and $R_{vv}$ remain fairly constant equal to 0.25 when $r_z/h$ ranges from $-2.5$ to 2.5. In addition, when the time lag $\tau$ is increased, the correlation coefficients show a periodic evolution locked on the period $T_s$ of the fundamental screech tone, and do not display significant variations with the spanwise separation $r_z$. These trends indicate that the oscillation mode of the shear-layer at the screech frequency has a two-dimensional structure. This instability is furthermore periodic and strongly correlated in time, which is consistent with the self-excitation due to the screech tones.

The space-time correlations in the downstream region of the jet are now investigated at $x/h = 22.5$. The axial velocity correlation $R_{uu}$ in figure 12.c is equal to 1 at $(r_z, \tau) = (0, 0)$. When the spanwise separation or the time lag are increased, the magnitude of $R_{uu}$ decreases, but the correlated region is larger than that observed for $x/h = 5$. Moreover, for $|r_z| > 1.25$ and $\tau > 0.5$, the correlation coefficient is close to 0 and the velocity perturbations are therefore weakly correlated. The downstream oscillation mode of the streamwise velocity component $u'$ is thus dominated by turbulent motions which do not exhibit any particular spatial or temporal properties. It is not the case for the correlation coefficient $R_{vv}$ of the transverse velocity which displays in figure 12.d a shape similar to that obtained for $x/h = 5$. The coefficient $R_{vv}$ is indeed periodic with the time lag $\tau$, and is fairly constant as the separation $r_z$ varies. In addition, the period of the phenomenon corresponds to the low frequency observed in the spectrum of figure 8.b, at Strouhal number St = 0.045. Note however that the correlation in the spanwise direction and in time are weaker than further upstream at

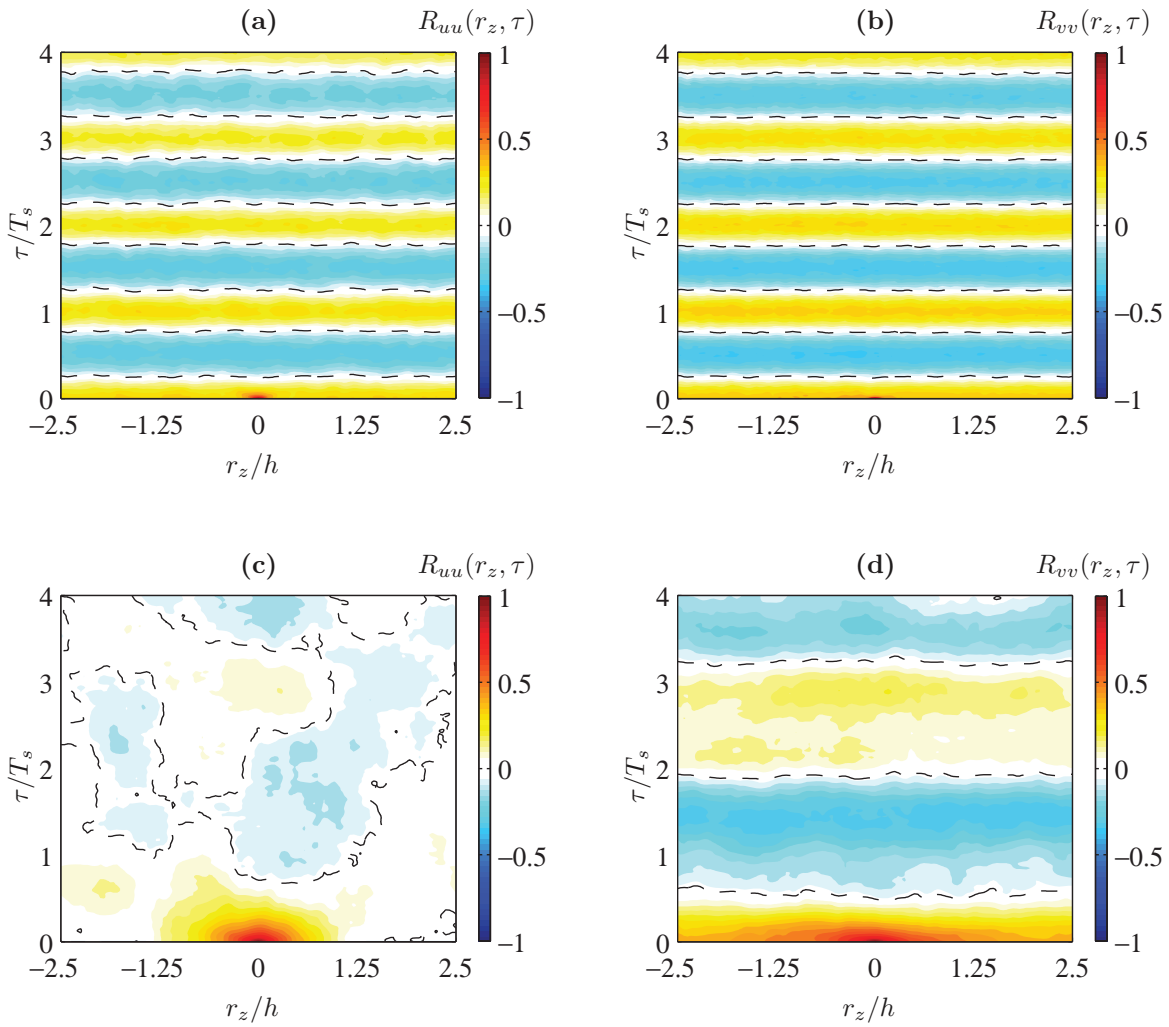


**Figure 12. Space-time correlation coefficients determined in the shear-layer as functions of the spanwise separation $r_z/h$ and the time lag $\tau/T_s$ normalized by the screech period. (a) $R_{uu}(r_z,\tau)$ at $x/h = 5$, (b) $R_{vv}(r_z,\tau)$ at $x/h = 5$, (c) $R_{uu}(r_z,\tau)$ at $x/h = 22.5$, and (d) $R_{vv}(r_z,\tau)$ at $x/h = 22.5$, along the line ($y = 0.5h, z = 0$). $- - -$ , $R_{uu}$ or $R_{vv} = 0$.**

$x/h = 5$. These results indicate that the downstream region of the jet displays a two-dimensional flapping mode, involving the transverse velocity $v'$.

## D. Acoustic field

### 1. *Upstream acoustic radiation*

The time evolution of the pressure signal at the upstream location $(x/h, y/h) = (-0.4, 0.85)$, represented by the point $P^+$ in figure 7, is plotted in figure 13 as a function of the time $t$, normalized by the screech period $T_s$. At the beginning of the computation, for $t/T_s < 30$, the upstream acoustic field shows a transient behavior. At time $t/T_s = 30$, the screech feedback is set up, and the pressure signal exhibits periodic oscillations up to the end of the computation, at time $t/T_s = 135$.

The power spectral density of the pressure perturbations close to the nozzle lip in $P^+$ is given in figure 14.a as a function of the Strouhal number $\mathrm{St} = fh/U_j$. A series of peaks are visible. The dominant tone is observed at $\mathrm{St} = 0.126$ and corresponds to the fundamental screech tone frequency. The other peaks are found to be the harmonics of the phenomenon and have a decreasing energy as the frequency increases. Remark that a non-harmonic peak can also be observed in figure 14.a at the Strouhal number 0.171. The presence of this

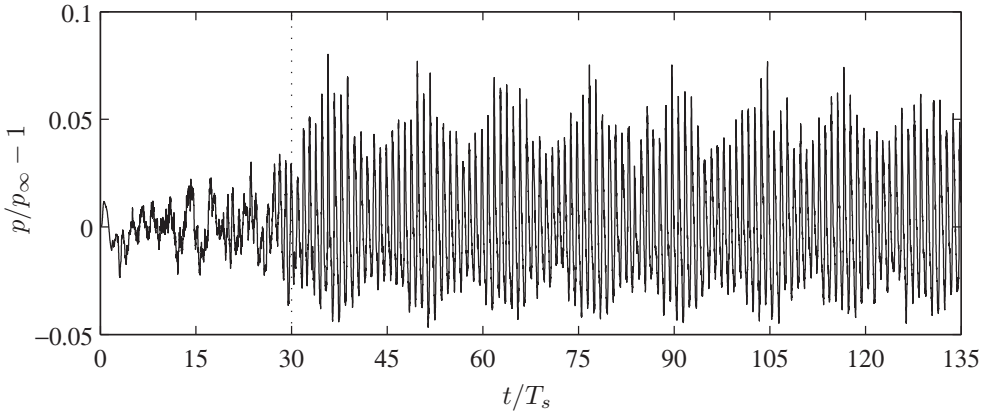


**Figure 13. Pressure history close to the nozzle lip, at $x/h = -0.4$ and $y/h = 0.85$. The dotted line represents the end of the transient period of the computation.**

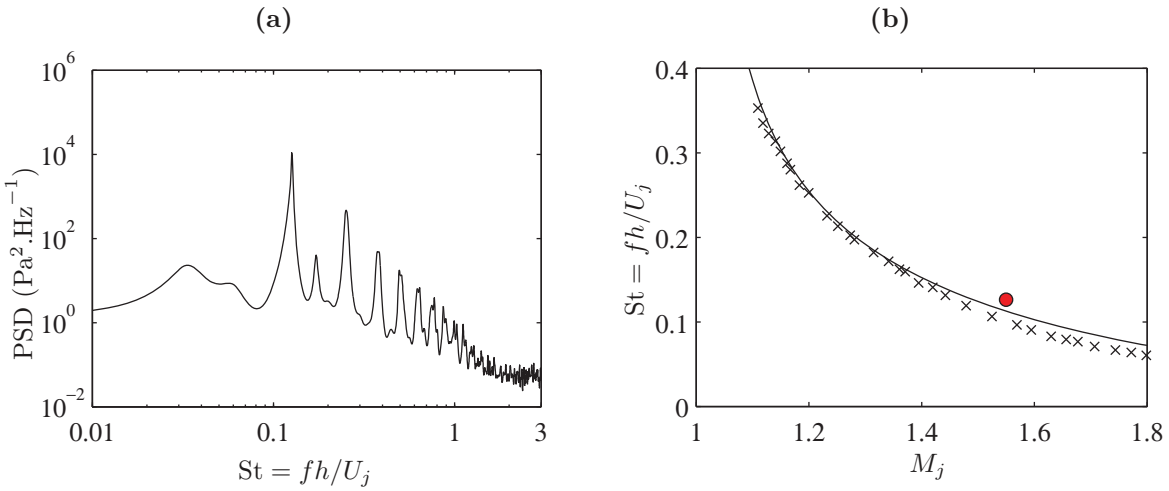


**Figure 14. (a), Power spectral density of the pressure fluctuations close to the nozzle lip, at $(x/h, y/h) = (-0.4, 0.85)$, as a function of the Strouhal number $\mathrm{St} = fh/U_j$. (b), Strouhal number $\mathrm{St} = fh/U_j$ of the fundamental screech tone as a function of the fully expanded jet Mach number $M_j$. Measurements on rectangular jets: ×, Panda *et al.*;[25] +, Raman & Rice.[24] ———, solution of Tam[26] for a planar jet ($u_c = 0.5U_j$). Present computation: ●.**

discrete frequency, which has not been reported in rectangular jet experiments, is difficult to explain. It is nevertheless interesting to note that this Strouhal number may be interpreted as the sum of the two dominant oscillation modes of the shear-layer reported for $v'$ in the downstream direction, shown in figure 8.b. Indeed, the low frequency mode occurs at St = 0.045 and the screech mode at St = 0.126, leading to a sum equal to 0.171. Nonlinear interactions between these two modes may thus contribute to the non-harmonic tone radiated in the upstream direction, but the mechanism of sound production has not been identified.

The Strouhal number of the fundamental discrete frequency is now represented in figure 14.b, where it is also plotted against the fully expanded jet Mach number for several experiments on rectangular jets, and where the analytical solution proposed by Tam[26] is shown for comparison. The screech Strouhal number provided by the LES is found to be slightly higher than experimental and theoretical results. Indeed, as pointed out in section B, the shock-cell spacing obtained by the LES is smaller than the experimental spacing, and an increased of the screech frequency may consequently be observed. Nevertheless, it should be noted that the screech Strouhal number predicted by the computation remains within 10% of the values measured on rectangular jets.

The sound pressure level (SPL) of the dominant screech tone is presented in figure 15 as a function of the fully expanded jet Mach number $M_j$, for the present computation and for the experiments of Panda *et al.*[25] on rectangular jets. A difference of 5 dB is visible between the SPL provided by the LES and

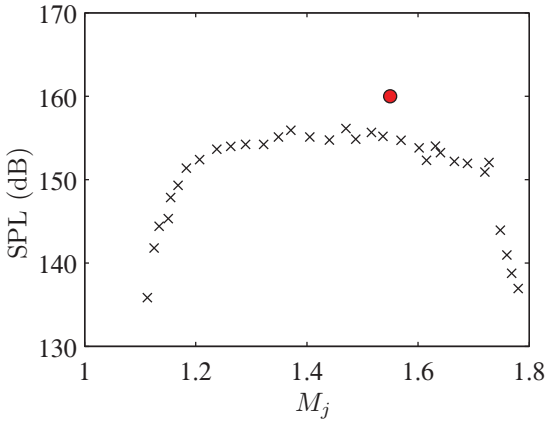


**Figure 15. Sound pressure level of the screech fundamental tone as a function of the fully expanded jet Mach number $M_j$. ×, Panda *et al.*[25] experiments on rectangular jets. Present computation: ●.**

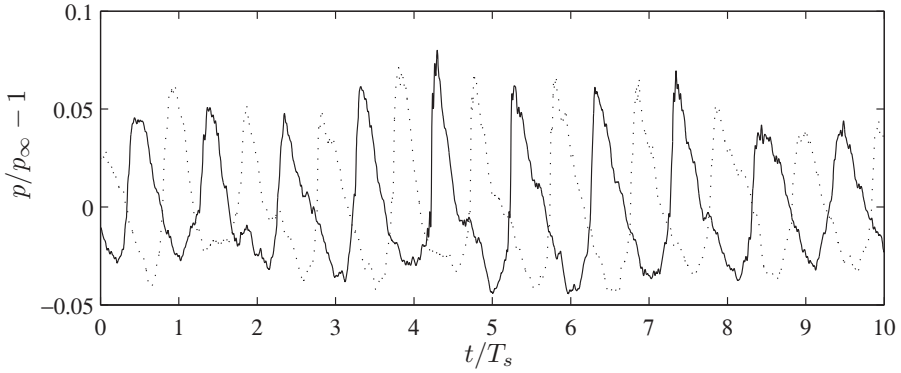


**Figure 16. Pressure history on either side of the jet in the upstream direction: ———, at $(x/h, y/h) = (-0.4, 0.85)$; at ····· , $(x/h, y/h) = (-0.4, -0.85)$.**

the SPL obtained in the experiments of Panda *et al.*[25] This discrepancy may be attributed to the shock strengths. Experimental results indeed suggest that the dominant screech sources are located for rectangular jets between the third and fourth shock cells.[28] However, as shown in section B, the planar geometry of the computation leads to shock strengths higher than those observed for rectangular jets, especially in the downstream direction. Although a connection between shock strength and screech amplitude has not been clearly settled so far,[28] this observation could explain the differences in figure 15.

Phase difference on either side of the jet is now investigated in the upstream direction, close to the nozzle exit. The time history of the pressure signals measured at the locations $(x/h, y/h) = (-0.4, 0.85)$ and $(x/h, y/h) = (-0.4, -0.85)$, represented by the points $P^+$ and $P^-$ in figure 7, are depicted in figure 16 for ten periods of the screech. The fluctuations at the two locations clearly seem to be correlated and in phase opposition. This trend is strongly supported by the computation of the cross-spectrum $P_{pp}$ between the two pressure probes $P^+$ and $P^-$. The corresponding amplitude $|P_{pp}|$, coherence function $C_{pp}$ and phase $\varphi_{pp}$ are respectively plotted in figure 17.a, 17.b and 17.c as functions of the Strouhal number $\mathrm{St} = fh/U_j$. Four harmonic peaks, corresponding to the screech tones, are visible on the cross-spectrum amplitude $|P_{pp}|$. Moreover, the coherence function $C_{pp}$ ensures that the pressure signals at the two observation points are correlated. The phase difference information finally indicates that the fundamental ($f_s$) and the second harmonic ($3f_s$) screech tones are antisymmetric, whereas the first ($2f_s$) and the third ($4f_s$) harmonics are symmetric. The quantity $\varphi_{pp}$ is indeed equal to $-\pi$ and $\pi$ at the frequencies $f_s$ and $3f_s$, and is null for $f = 2f_s$ and $f = 4f_s$. These results are in agreement with the measurements of Raman & Rice[24] who observed that the upstream acoustic field generated by a rectangular jet is antisymmetric for the fundamental screech tone, symmetric for the first harmonic and antisymmetric for the second harmonic.

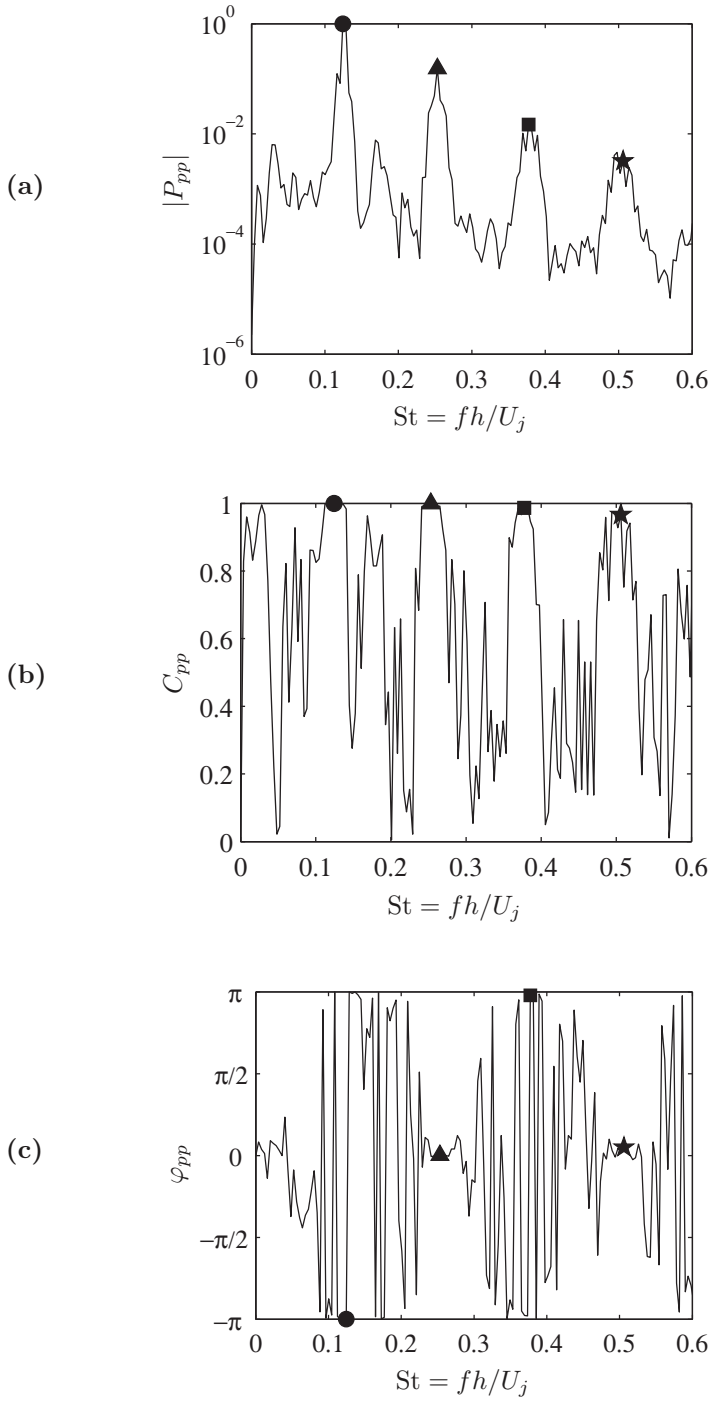


**Figure 17. Cross-spectrum of the pressure fluctuations in the upstream direction, on either side of the jet, in $(x/h, y/h) = (-0.4, 0.85)$ and $(x/h, y/h) = (-0.4, -0.85)$), as functions of the Strouhal number St $= fh/U_j$. •, Screech fundamental frequency ($f_s$); ▲, 1st harmonic ($2f_s$); ■, 2nd harmonic ($3f_s$); ⋆, 3rd harmonic ($4f_s$). (a), Amplitude $|P_{pp}|$; (b), coherence function $C_{pp}$; (c), phase $\varphi_{pp}$.**

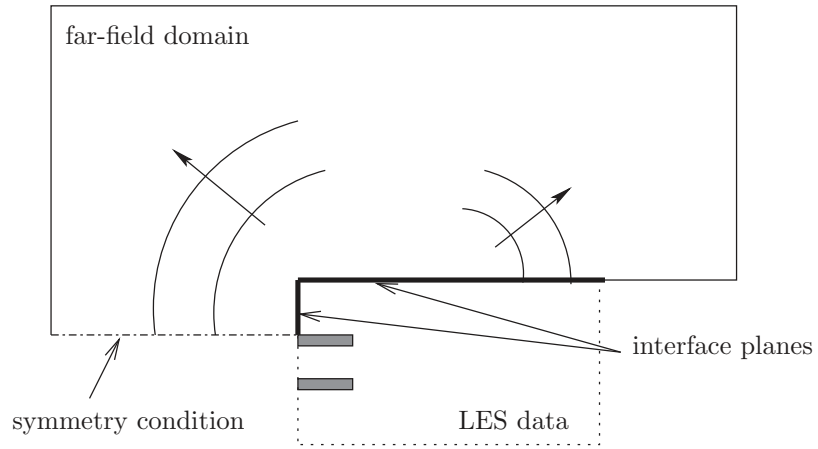


**Figure 18. Schematic view of the extrapolation domain and of the interface planes used to introduce the LES data into the far-field computation.**

*2. Far-field extrapolation*

A hybrid zonal approach is implemented to predict the far-field noise. In this way, the near-field data provided by the LES computation are extrapolated using a simplified set of equations, allowing long-range propagation of acoustic waves.

In the present work, the three-dimensional equations of linear acoustics are solved beyond an extrapolation surface, where the LES near-field is specified. Assuming that time-dependent perturbations are small and that the surrounding medium is at rest, keeping only the first order terms in the Euler equations yields the linear acoustic equations:

$$\frac{\partial \mathbf{U}'}{\partial t} + \frac{\partial \mathbf{E}'}{\partial x} + \frac{\partial \mathbf{F}'}{\partial y} + \frac{\partial \mathbf{G}'}{\partial z} = 0 \tag{6}$$

where,

$$\begin{aligned} \mathbf{U}' &= [\rho', \quad \rho_\infty u', \quad \rho_\infty v', \quad \rho_\infty w'] \\ \mathbf{E}' &= [\rho_\infty u', \quad p', \quad 0, \quad 0] \\ \mathbf{F}' &= [\rho_\infty v', \quad 0, \quad p', \quad 0] \\ \mathbf{G}' &= [\rho_\infty w', \quad 0, \quad 0, \quad p'] \end{aligned} \tag{7}$$

The mean flow variables are $\rho_\infty$ and $p_\infty$ for the density and the pressure. Pressure fluctuations can then be computed thanks to the relationship $p' = c_\infty^2 \rho'$, where $c_\infty = \sqrt{\gamma p_\infty / \rho_\infty}$ is the mean sound speed, and the specific heat ratio is $\gamma = 1.4$.

The numerical methods used to solve equation (6) are identical to those of the LES. Low dispersion and low dissipation explicit numerical algorithms[14,15] and non-reflecting conditions[20] are thus implemented for space and time discretizations. The domain is periodic in the spanwise direction. The time step is doubled compared to LES and the mesh size is six times larger. The computational domain contains the volume $[-35h, 45h] \times [0, 45h] \times [-2.5h, 2.5h]$.

The flow variables issued from the LES are introduced into the far-field computation at two interface planes, as shown schematically in figure 18. The first plane lies in the directions $x$ and $z$ and is situated on the top of the domain at $y/h = 7$, while the second is in the $(y, z)$-plane at $x/h = -0.4$ and is used to take into account the acoustic field radiated in the upstream direction. Furthermore, to reduce diffraction effects due to the end of the vertical plane close to the nozzle, a symmetry condition is enforced at the bottom of the far-field grid.

A snapshot of instantaneous pressure in the central $(x, y)$-plane is depicted in figure 19. The radiation of the fundamental screech tone appears in the upstream direction where periodic low-frequency wavefronts are observed. On the contrary, downstream and sideline acoustic fields seem to be dominated by a broader frequency range, containing in particular wavelengths shorter to that of the screech. It should be however noted that the data provided by the far-field extrapolation are not relevant for low angles of observation

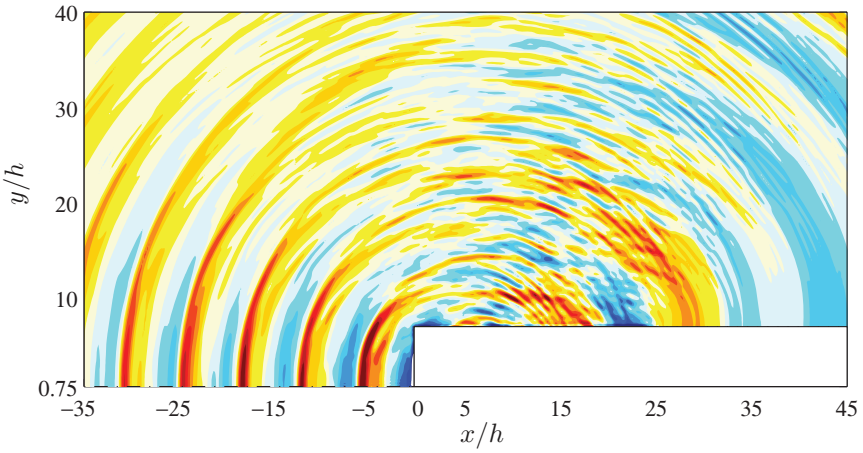


**Figure 19. Snapshot of instantaneous pressure in the central $(x, y)$-plane obtained with the far-field extrapolation. Colorscale from $-0.025p_\infty$ to $0.025p_\infty$.**

($< 30°$). The interface $(x, z)$-plane indeed extends over $0 < x/h < 25$, whereas the far-field is computed up to $x/h = 45$. A shadow zone therefore appears for $x/h > 25$ in the vicinity of the bottom of the domain.

The power spectral densities of the pressure fluctuations are computed for various positions in the far-field. Measurement points are located in the central $(x, y)$-plane, on a circle of radius $35h$ centered on the position $(x/h, y/h) = (6, 0)$, which is close to the third shock-cell. The angle of observation with respect to the downstream direction is denoted $\theta$. Power spectral densities are plotted in figure 20 as functions of the Strouhal number $\mathrm{St} = fh/U_j$, for $\theta = 155°$, $\theta = 80°$ and $\theta = 40°$. In the upstream direction, for $\theta = 155°$, the pressure spectrum is dominated by the screech harmonics and is similar to the spectrum of figure 14.a, computed in the vicinity of the nozzle. In the sideline direction, for $\theta = 80°$, screech fundamental tone is no longer visible whereas the first harmonic has the largest amplitude. Furthermore, two broadband peaks are noticeable. One occurs at Strouhal number $\mathrm{St} \simeq 0.07$ and may be associated with the mixing noise generated by the large turbulent structures. The second peak is located between $\mathrm{St} = 0.1$ and $\mathrm{St} = 0.2$ and is attributed to shock-associated noise. Further downstream, for $\theta = 40°$, turbulent mixing noise is the principal component of the acoustic field. A dominant peak centered on Strouhal number $\mathrm{St} \simeq 0.07$ is indeed observed in the spectrum.

These observations are supported by figure 21 which represents a colormap of the power spectral density of the pressure fluctuations in the far-field in logarithmic scale, as a function of the Strouhal number $\mathrm{St} = fh/U_j$ and of the angle of observation $\theta$ with respect to the downstream direction. Also shown in the figure is the predicted central frequency of shock-associated noise based on the model of Tam.[33] The fundamental screech tone appears to radiate in the upstream direction (for instance at $\theta \simeq 150°$ and $\mathrm{St} \simeq 0.13$) whereas the first harmonic dominates other noise sources in the sideline direction, for $\theta \simeq 80°$. Moreover, the mixing noise generated by large scale structure emerges in the downstream direction, for $\theta < 70°$, at a Strouhal number close to 0.07. Shock-associated noise is especially visible in the region $50° < \theta < 130°$ where a broadband peak is seen with a central frequency varying with the angle of observation. In addition, the evolution of this central frequency with $\theta$ is in agreement with the prediction of Tam.[33] The acoustic far-field extrapolated from the LES computation is thus in qualitative agreement with experimental data.[34]

Screech tones directivity patterns are now computed using the data provided by the far-field extrapolation. For comparison, screech directivity is also determined using a phased array of acoustic monopoles.[35] A series of sources, situated at the end of the shock-cells, whose relative phases are given by the convection process, radiate in far-field some pressure fluctuations which can be written as,

$$p = \exp\left[\frac{2i\pi(c_\infty t - r_0)}{\lambda_n}\right] \sum_j \frac{S_j}{r_j} \exp\left[-2i\pi j \frac{L_s}{\lambda_n}\left(\frac{1}{M_c} - \cos\theta\right)\right] \tag{8}$$

where $L_s$ is the shock spacing, $r_0$ is the distance between the observation point and the reference location $(x/h, y/h) = (6, 0)$, $r_j$ is the separation between the observation point and the source $j$, $S_j$ is the amplitude

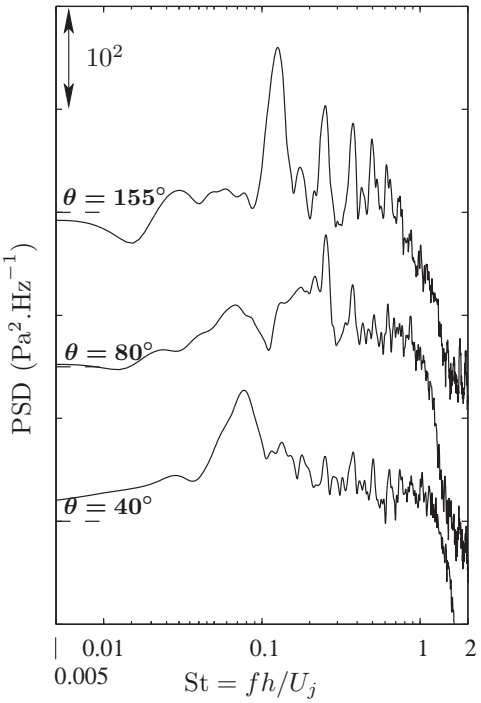


**Figure 20. Power spectral density of the pressure fluctuations in the far-field as a function of the Strouhal number St $= fh/U_j$, for various angles of observation $\theta$ with respect to the downstream direction. From the top : $\theta = 155°$, $\theta = 80°$ and $\theta = 40°$.**

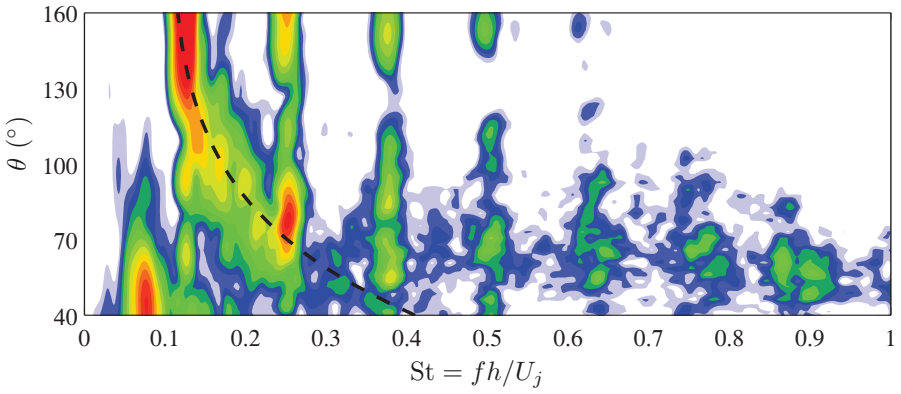


**Figure 21. Colormap of the power spectral density of the pressure perturbations in the far-field as a function of the Strouhal number St $= fh/U_j$ and of the angle of observation $\theta$ with respect to the downstream direction (logarithmic colorscale). − − − , prediction of the central frequency of shock-associated noise.[33]**

of the source $j$, and $\lambda_n$, the wavelength of the $n$-th screech harmonic, is given by the model of Tam:[26]

$$\lambda_n = \frac{L_s}{n}\left(1 + \frac{1}{M_c}\right) \tag{9}$$

The convective Mach number is taken to be equal to $0.55U_j/c_\infty$, and $\theta$ is the polar angle with respect to the downstream direction. The present study makes use of six sources with the following arbitrary amplitudes: $(S_1, \ldots, S_6) = (0.5, 0.5, 1, 0.5, 0.25, 0.25)$, the third shock-cell being the dominant source. Recall that measurement points are located in the central $(x, y)$-plane, on a circle of radius $35h$ centered on $(x/h, y/h) = (6, 0)$.

Both numerical and analytical directivities are reported as functions of angle $\theta$ in figures 22.a, 22.b and 22.c for the fundamental tone, the first harmonic and the second harmonic, respectively. In all figures, the

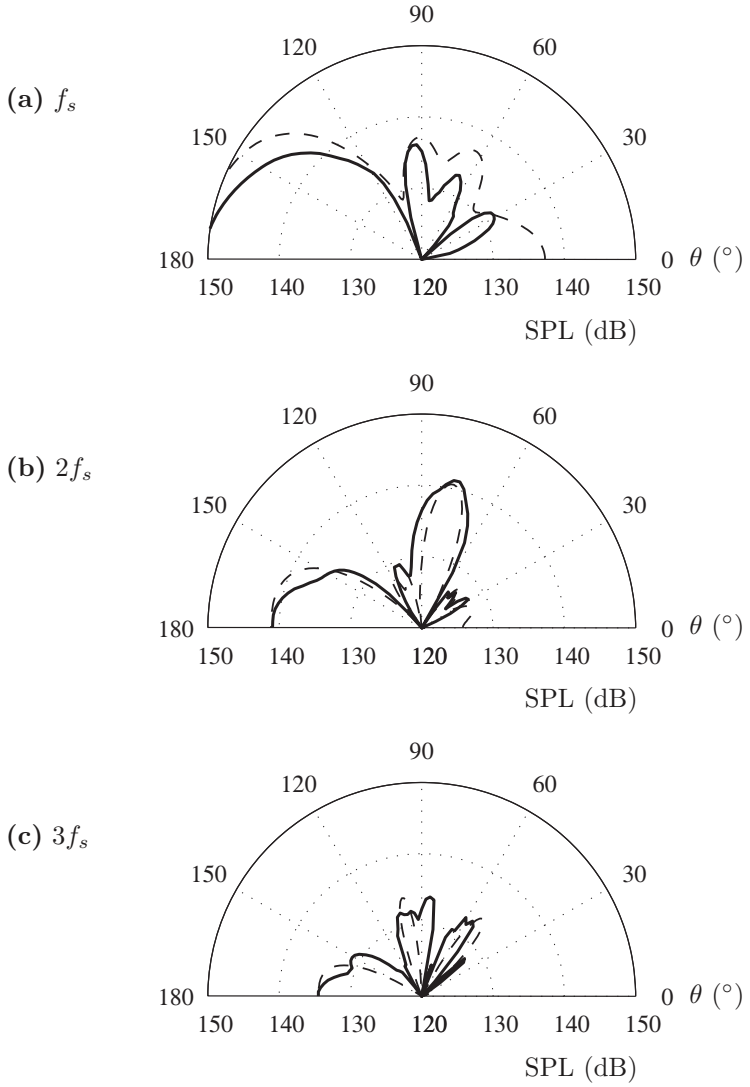


**Figure 22. Far-field directivity of screech tones. Sound pressure level (SPL) as a function of the angle of observation $\theta$ with respect to the downstream direction. ——— , far-field extrapolation ; − − − , prediction by a phased array of monopoles. (a) Screech frequency ($f_s$), (b) 1st harmonic ($2f_s$), (3) 2nd harmonic ($3f_s$).**

radiation patterns appear to collapse rather well for $\theta > 30°$. Indeed, lobe positions and relative amplitudes obtained by the extrapolation of the LES data and by the phased array of monopoles are seen to agree quite well. The fundamental screech tone exhibits a dominant lobe in the upstream direction and two secondary lobes in the sideline direction. As for the first harmonic, two lobes of equal amplitudes are noticeable, one around $\theta \sim 80°$ and an other with a larger width in the upstream direction. Finally, the second harmonic displays three lobes, the wider lobe being oriented toward $\theta = 180°$. As expected, for small angles, the pressure field in the shadow zone does not agree with the prediction of (8). This trend is especially visible for the fundamental tone in figure 22.a.

## IV. Flow visualizations: shock/vortex interactions

Shock/vortex interactions are now investigated to highlight the screech sound production mechanisms. The flow motions are visualized by plotting contour maps of the density gradient modulus $|\boldsymbol{\nabla}\rho|$ in the central $(x, y)$-plane. The method, commonly referred to as numerical Schlieren, allows us in particular to identify the location of the shocks, where strong gradients of the flow variables are observed. Such a visualization is provided in figure 23 which presents an overview of the flow field in the central $(x, y)$-plane. Pressure

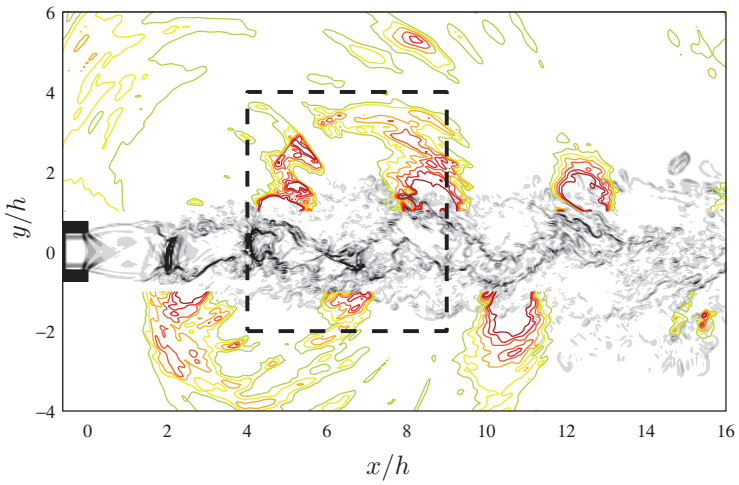


**Figure 23. Overview of the flow field and of the acoustic near field in the central $(x, y)$-plane. The density gradient modulus $|\nabla\rho|$ is plotted in gray (grayscale between 0 and $6\rho_\infty/h$), and pressure iso-contours are represented in the near-field (colorscale from $p_\infty$ to $1.1p_\infty$).**

iso-contours are also shown in the near-field. Wavefronts propagating in the upstream direction are visible on either side of the jet and correspond to the screech. Furthermore, the third compression shock, which is located around $x/h = 6.5$, seems to be the origin point of these sound waves. The flow visualization study will therefore now focus on a region surrounding the third shock-cell, whose limits are given by the dashed rectangle in figure 23. Visualizations of shock/vortex interaction are provided in figure 24 for this region. Also shown in the figure is the upper part of the acoustic near field. Half a period of the screech cycle is depicted from figure 24.1 to figure 24.9.

### Coherent structures

As stated above, the numerical Schlieren allows to locate shock positions, but strong density gradients also takes place in regions of the flow that are significantly sheared, like in the jet frontier. This behavior is illustrated for instance in figure 24.1 where dark regions are visible in the streamwise direction and highlight the sinuous shape of the jet, which is due to the flapping motion induced by the screech self-excitation. Also observed in the figure are the coherent vortical structures associated with the screech tones excitation. The blue arrows represent the rotation and the convection of a structure located in the lower part of the jet, at $(x/h, y/h) \simeq (6.5, -1)$. Two similar structures may be seen in the upper shear-layer: one is near $(x/h, y/h) \simeq (4, 1)$ and an other near $(x/h, y/h) \simeq (9, 1)$. Note that these vortices are organized in an antisymmetric manner, and that low-vorticity regions are found between them, as it is shown for instance at $(x/h, y/h) \simeq (6.5, 1)$ by the blue cross. These saddle points are of importance because shock-leakage is expected to occur in their vicinity.[3] A comparative study of the figures also shows the convection process. For example, the vortex in figure 24.1 located at $(x/h, y/h) \simeq (6.5, -1)$ moved to the position $(x/h, y/h) \simeq (9, -1)$ after half a period of the screech in figure 24.9. One may also remark that in figure 24.9 flow organization is antisymmetric compared to figure 24.1. The blue arrows of figure 24.9 represents in particular a structure antisymmetric to the structure in figure 24.1.

### Shock motion

Flow visualizations in figures 24.1–24.9 give in addition the opportunity for investigating shock motions of the third shock-cell, which is represented by a light blue dashed line. In all the figures, the shock remains located between $x/h = 6$ and $x/h = 7$, and shows a rotating motion. In figure 24.1, the shock is oblique and situated around $x/h = 6.5$. In figure 24.2 the shock is still close to $x/h = 6.5$, but the upper tip of the shock has moved upstream and the lower tip downstream. This rotating motion is represented by the two light blue arrows in figure 24.2. The other figures (24.3 to 24.9) show that this motion carries on through the rest of the cycle, and leads to a shock-cell pattern in figure 24.9 antisymmetric to that of figure 24.1: the shock in figure 24.9 is located at $x/h = 6.5$ and exhibits an oblique shape, but with a slope opposite to that

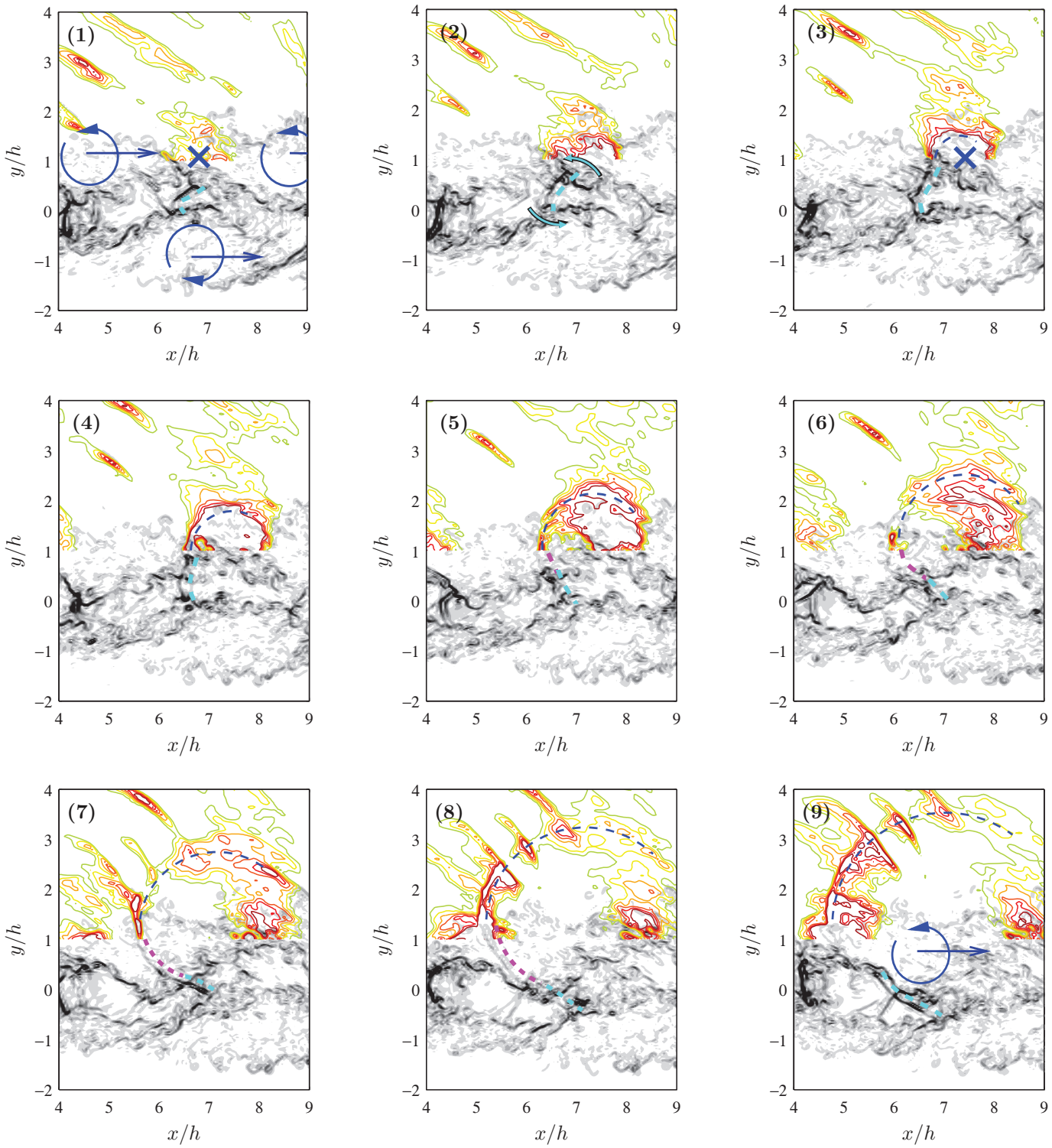


**Figure 24.** Visualizations of the flow field and of the acoustic near field in the central $(x, y)$-plane, during half a period of the screech loop. The density gradient modulus $|\nabla\rho|$ is plotted in gray (grayscale between 0 and $6\rho_\infty/h$), and pressure iso-contours are represented in the near-field (colorscale from $p_\infty$ to $1.1p_\infty$). From (1) to (9): $t/T_s = 0,\ 1/16, \ldots,\ 7/16,\ 8/16$, where $T_s$ is the screech period. - - - -, shock; - - - -, sound wave generated by the shock-leakage phenomenon; - - - -, rotating density gradient. ↻, coherent structure. ×, low-vorticity region.

in figure 24.1.

**Sound generation**

The sound generation mechanisms are now investigated in term of the shock-leakage phenomenon. The focus is therefore brought into the interactions between the compression shock and the low-vorticity region initially located at $(x/h, y/h) \simeq (6.5, 1)$ in figure 24.1. The flow motion implies that the low-vorticity region is convected downstream while the upper tip of the shock moves upstream. The low vorticity region and the shock tip are seen to interact in figure 24.3, and the coupling results in the production of an acoustic wavefront which is represented by a dashed blue line. Recall that the shock-leakage mechanism proposed by Suzuki & Lele[3] states that the shock leaks through the shear-layer near the saddle points of vorticity, and creates a pressure gradient that propagates in the near-field with a nearly circular wavefront, covering a wide range of angles including the upstream direction. This sound generation mechanism is observed in figures 24.3–24.9, where the wavefront generated in 24.3 visibly forms a circular sound wave propagating in the upstream direction. The maximum amplitude moreover occurs in this direction.

Another aspect of the geometrical interpretation of Suzuki & Lele[3] of the shock/vortex interaction is the rotating effect of local vorticity on the wavefront normal. This behavior can be observed in the flow visualizations in the present work. Indeed, it has been shown above that the compression shock leaks through the shear-layer, but it seems in addition that the shock generates a wave which is trapped inside the vortical structure. The phenomenon is apparent in figures 24.5–24.9, where a strong density gradient represented by a magenta dashed line is seen in the core of a coherent structure. The wavefront moves upstream, but remains inside the vortex due to its rotating motion.

## V. Conclusion

In the present paper, the compressible large eddy simulation of a three-dimensional planar underexpanded jet is performed using explicit selective filtering with spectral-like resolution, and low dispersion and low dissipation numerical methods. The investigation of the numerical results demonstrates that the computation correctly reproduces the screech tone generation phenomenon, which shows the feasibility of the direct noise computation of such a feedback loop with high-order algorithms. Flow visualizations of the third-shock cell motions finally provided evidences that shock-leakage occurs in between coherent vortices associated with the screech excitation, resulting in the production of upstream-propagating sound waves.

## Acknowledgments

This work was done in the framework of the "Noise Generation in Turbulent Flows" project initiated by DFG/CNRS. The authors gratefully acknowledge the Institut du Développement et des Ressources en Informatique Scientifique (IDRIS - CNRS) for providing computing time.

## References

[1]Powell, A., On the mechanism of choked jet noise, *Proc. Royal Society of London*, Series B, **66**, pp. 1039-1056, 1953.

[2]Raman, G., Supersonic jet screech: half-century from Powell to the present, *J. Sound Vib.*, **225**, pp. 543-571, 1999.

[3]Suzuki, T., Lele, S.K., Shock leakage through an unsteady vortex-laden mixing layer: application to jet screech, *J. Fluid Mech.*, **490**, pp. 139-167, 2003.

[4]Shen, H., Tam,C.K.W., Three-dimensional numerical simulation of the jet screech phenomenon, *AIAA J.*, **40**(1), pp. 33-41, 2002.

[5]Bogey, C., Bailly, C., Juvé D., Noise investigation of a high subsonic, moderate Reynolds number jet using a compressible LES, *Theor. Comput. Fluid Dyn.*, **16**, pp. 273-297, 2003.

[6]Bogey, C., Bailly, C., Investigation of downstream and sideline subsonic jet noise using large eddy simulation, *Theor. Comput. Fluid Dyn.*, **20**(1), pp. 23-40, 2006.

[7]Bogey, C., Bailly C., Large eddy simulations of transitional round jets: influence of the Reynolds number on flow development and energy dissipation, *Phys. Fluids*, in press, 2006.

[8]Bodony, D.J., Lele, S.K., 2005, On Using Large-Eddy Simulation for the Prediction of Noise from Cold and Heated Turbulent Jets, *Phys. Fluids*, **17**, #085103, 2005.

[9]Al-Qadi, I.M.A., Scott, J.N., High-order three-dimensional numerical simulation of a supersonic rectangular jet, *9th AIAA/CEAS Aeroacoustics Conference*, May 12-14, Hilton Head, South Carolina, USA, AIAA Paper 2003-3238, 2003.

[10]Imamoglu, B., Balakumar, P., Three dimensional computation of shock induced noise in imperfectly expanded supersonic jets, *9th AIAA/CEAS Aeroacoustics Conference*, May 12-14, Hilton Head, South Carolina, USA, AIAA Paper 2003-3249, 2003.

[11]Loh, C.Y., Himansu, A., Hultgren, L.S., A 3-D CE/SE Navier-Stokes solver with unstructured hexahedral grid for computation of nearfield jet screech noise, *9th AIAA/CEAS Aeroacoustics Conference*, May 12-14, Hilton Head, South Carolina, USA, AIAA Paper 2003-3207, 2003.

[12]Garnier, E., Mossi, M., Sagault, P., Comte, P., Deville, M., On the use of shock-capturing schemes for large-eddy simulation, *J. Comput. Phys.*, **153**, pp. 273-311, 1999.

[13]Ghosal, S., An analysis of numerical errors in large-eddy simulations of turbulence, *J. Comput. Phys.*, **125**, pp. 187-206, 1996.

[14]Bogey, C., Bailly, C., A family of low dispersive and low dissipative explicit schemes for flow noise and noise computations, *J. Comput. Phys.*, **194**, pp. 194-214, 2003.

[15]Berland, J., Bogey, C., Bailly, C., Low-dissipation and low-dispersion fourth-order Runge-Kutta algorithm, *Computers and Fluids*, in press, 2006.

[16]Bogey, C., Bailly C., Large eddy simulations of round free jets using explicit filtering with/without dynamic Smagorinsky model, *Int. J. Heat Fluid Flow*, in press, 2006.

[17]Vreman, B., Geurts, B., Kuerten, J.G.M., Subgrid-modeling in LES of compressible flow, *Applied Scient. J.*, **54**, pp. 191-203, 1995.

[18]Bogey, C., Bailly C., Decrease of the effective Reynolds number with eddy-viscosity subgrid-scale modeling, *AIAA J.*, **43**(2), pp. 437-439, 2005.

[19]Rizzetta, D.P., Visbal, M.R., Blaidell G.A., A time-implicit compact differencing and filtering scheme for large-eddy simulation, *Int. J. Numer. Meth. Fluids*, **42**(6), pp. 665-693, 2003.

[20]Tam, C.K.W., Dong, Z., Radiation and outflow boundary conditions for direct computation of acoustic and flow disturbances in a nonuniform mean flow, *J. Comput. Ac.*, **4**(2), pp. 175-201, 1996.

[21]Poinsot, T.J., Lele, S.K., Boundary conditions for direct simulations of compressible viscous flows, *J. Comput. Phys.*, **101**, pp. 104-129, 1992.

[22]Krothapalli, A., Hsia, Y., Baganoff, D. Karamcheti, K., The role of screech tones in mixing of an underexpanded rectangular jet, *J. Sound Vib.*, **106**(1), pp. 119-143, 1986.

[23]Zaman, K.B.M.Q., Far-field noise of a subsonic jet under controlled excitation, *J. Fluid Mech.*, **152**, pp. 83-111, 1985.

[24]Raman, G., Rice, E.J., Instability modes excited by natural screech tones in a supersonic rectangular jet, *Phys. Fluids*, **6**(12), pp. 3999-4008, 1994.

[25]Panda, J., Raman, G., Zaman, K.B.M.Q., Underexpanded screeching jets from circular, rectangular and elliptic nozzles, *3rd AIAA/CEAS Aeroacoustics Conference*, May 12-14, Atlanta, GA, USA, AIAA Paper 1997-1623, 1997.

[26]Tam, C.K.W., The shock-cell structures and screech tone frequencies of rectangular and non-axisymmetric supersonic jets, *J. Sound Vib.*, **121**(1), pp. 135-147, 1998.

[27]Morris, P.J., Bhat, T.R.S., Chen G., A linear shock cell model for jets of arbitrary exit geometry, *J. Sound Vib.*, **132**(2), pp. 199-211, 1989.

[28]Raman, G., Cessation of screech in underexpanded jets, *J. Fluid Mech.*, **336**, pp. 69-90, 1997.

[29]Raman, G., Screech tones from rectangular jets with spanwise oblique shock-cell structures, *J. Fluid Mech.*, **330**, pp. 141-168, 1997.

[30]Gutmark, E., Wygnanski, I., The planar turbulent jet, *J. Fluid Mech.*, **73**(3), pp. 465-495, 1976.

[31]Bradbury, L.J.S., The structure of a self-preserving turbulent plane jet, *J. Fluid Mech.*, **23**(1), pp. 31-64, 1965.

[32]Thomas, F.O., Prakash, K.M.K., An experimental investigation of the natural transition of an untuned jet, *Phys. Fluids A*, **3**, pp. 90-105, 1991.

[33]Tam, C.K.W., Stochastic model theory of broadband shock associated noise from supersonic jets, *J. Sound Vib.*, **116**(2), pp. 265-302, 1987.

[34]Tam, C.K.W., Supersonic jet noise, *Annu. Rev. Fluid Mech.*, **27**, pp. 17-43, 1995.

[35]Norum, T.D., Screech suppression in supersonic jets, *AIAA J.*, **21**(2), pp. 235-240, 1983